Yang, H., et al., 2022, Crustal transpressional fault geometry influenced by viscous lower crustal flow: Geology, v. 50, https://doi.org/10.1130/G50061.1

Crustal transpressional fault geometry influenced by viscous lower crustal flow

Haibin Yang[1,2], Louis N. Moresi[1], Mark Quigley[2,3], Metin Kahraman[4], Doğan Kalafat[5]

[1]*Research School of Earth Sciences, Australian National University, Canberra, Australia*

[2]*School of Earth Sciences, University of Melbourne, Victoria, Australia*

[3]*Seismology Research Centre, Richmond 3121, Victoria, Australia*

[4]*Eurasia Institute of Earth Sciences, Istanbul Technical University, Istanbul, Turkey*

[5]*Kandilli Observatory and Earthquake Research Institute, Boğaziçi University, Çengelköy-Istanbul, Turkey*

Corresponding author: Haibin Yang

Email: haibin.yang@anu.edu.au

Methods

Governing equations

We simulate fault evolution by using the open-source software Underworld (Mansour et al., 2020), which is based on the particle-in-cell, finite element algorithm (Moresi et al., 2007). The Underworld software solves equations for conservation of momentum (1a) and mass (incompressible material, 1b), and the calculated velocity field are coupled in temperature calculation with advection-diffusion equation (1c):

$$\nabla \cdot \sigma - \nabla P = \rho g \tag{1a}$$

$$\nabla \cdot u = 0 \tag{1b}$$

$$\rho C_p \left(\frac{\partial T}{\partial t} + u \cdot \nabla T\right) = \frac{\partial}{\partial x_i}\left(k \frac{\partial T}{\partial x_i}\right) + \rho H \tag{1c}$$

where σ denotes deviatoric stress, P pressure, ρ density, g gravitational acceleration, u velocity, T temperature, V velocity, C_p heat capacity, k thermal conductivity, H the heat production. The heat source only considers radioactive decay, and heating caused by shear, adiabatic, or melt processes are excluded in modelling.

Rheology

The viscoplastic rheology is applied in the numerical calculation. The viscous deformation is represented by the dislocation creep power law:

$$\dot{\varepsilon}_{II} = A\, {\sigma_{II}}^{n}\, exp\left(-\frac{E + VP}{RT}\right) \tag{2}$$

where $\dot{\varepsilon}_{II}$ and σ_{II} are the square root of the second invariant of strain rate and deviatoric stress, respectively, n stress exponent, E activation energy, V activation volume, R the gas constant and A material constant. The Drucker-Prager pressure-dependent criteria is used for plastic deformation

$$\sigma_{yield} = \mu P + C \tag{3}$$

with σ_{yield} the maximum second deviatoric stress invariant, μ friction coefficient and C cohesion. Linear strain weakening of friction coefficient (0.4-0.1) and cohesion (20-5 MPa) between plastic strain of 0.5 and 1.5 is applied. The composite viscoplastic flow material is modelled with an effective viscosity: $\eta_{vp} = min\left(\frac{\sigma_{II}}{2\dot{\varepsilon}_{II}}, \frac{\sigma_{yield}}{2\dot{\varepsilon}_{II}}\right)$, which is limited in the range between 10^{18} Pa·s and 10^{24} Pa·s. Parameters used in this study are listed in Table S1.

3D Model setup

The model domain has total dimensions of 600 × 300 ×120 km with 240×144×48 linear, quadrilateral elements. The 120-km-thick model consists of a 30-km-thick crust and a 90-km-thick mantle (Fig. 1 in main text). Based on a regional tectonic interpretation and geophysical observations (Atwater and Stock, 1998; Wang et al., 2020), the calculation domain is divided into 3 tectonic blocks: the coast area (west of SAF), the Great Valley block (east of SAF and north of the Garlock Fault), and the Sierra Nevada-Mojave (east of SAF and south of the Garlock fault) (Fig.1 in main text). Seismic surveys show that the crustal thickness in most of the SAF system varies between 25-35 km thick (Fliedner et al., 1996; Howie et al., 1993; Jones et al., 1994; Mooney and Weaver, 1989; Zhu and Kanamori, 2000). We set a constant value of 30 km for crustal thickness and neglect lateral variations. The SAF is pre-defined as vertical weak zone of 10 km width and the Big Bend of the fault near the western Transverse Range is an initial condition in our model (Fig. 1).

The 4-6 Ma near-fault block uplift of the San Emigdio Mountains along the Big Bend indicated from low-temperature thermochronology studies (Niemi et al., 2013) may be attributed to the intensive transpressional strain near the Big Bend. In this case, we assume that the Big Bend has formed when the model begins, though the exact time or mechanism for the formation of Big Bend is debated (Niemi et al., 2013; Popov et al., 2012). The weak zone is initially represented by materials with plastic strain of 2, which is the upper limit of the linear strain weakening, and the corresponding effective cohesion and friction coefficient are 5 MPa and 0.1, respectively. A minimum friction coefficient of 0.02 is also tested and did not affect conclusions derived in this study. This friction coefficient of 0.02 produces a weak fault as observed in regional stress mapping and laboratory experiments (Collettini et al., 2009; Zoback et al., 1987).

The fault plane is assumed to be vertical everywhere along the fault strike but can deform with time. The fault extends into the mantle to a depth of 60 km as the deep-penetrating fault induced narrow shear zone in shallow mantle is imaged by conversion of S to P waves from lithosphere base (Ford et al., 2014). A 50-km-wide and 60-km-deep buffer zone is added to both ends of the model to minimize artificial boundary effects. The trackers of the fault plane are passive particles that are initially set in the middle part of the weak zone and are allowed to move within the model during particle advection. The buffer zone has a relatively weak viscosity of 10^{20} Pa·s; this value is applied to all material particles that enter the buffer zone.

Continental crust is generally composed of felsic upper crust and mafic lower crust (Burgmann and Dresen, 2008), but many seismic studies indicate an absence of mafic lower crust in the Mojave block. A receiver function study found the Vp/Vs ratio < 1.75, indicating a felsic crust (Zhu and Kanamori, 2000). A seismic refraction survey (Fuis et al., 2001) detected the seismic P wave velocity in the lower crust to be 6.3 km/s. This is unusually low: mafic lower crust generally has a P wave velocity of > 6.5 km/s. which might be caused by removal of mafic lower crust which may be linked to early Miocene magmatism (ca. 22-24 Ma) (Glazner et al., 2002). The southeast Sierra Nevada is also thought to have lost its mafic crustal root (Fliedner et al., 1996; Jones et al., 1994), and the delamination is estimated to occur ca. 3.5 Ma, which is evidenced by Pliocene emplacement of mafic potassic magmatism (Manley et al., 2000). Therefore, both the Mojave and Sierra Nevada block are assumed in our models to have no mafic lower crustal layer.

The model evolution time in our numerical experiments is < 4 Myr. Because the relative motion direction between the North American plate and Pacific plate has not significantly changed (<5 degree) since 8 Ma (Atwater and Stock, 1998), the boundary conditions in our model do not vary with time. A constant shear velocity (V_x) of 40 mm

yr^{-1} is applied on the back plane (y = 300 km) while the velocity in the front plane (y = 0 km) is zero. Free slip conditions are applied to the other boundaries. The initial condition for the temperature field assumes a half-space cooling model for a oceanic plate cooling after 50 Myr (Chapter 4.16; Turcotte and Schubert (2002)). The resulting temperature at the Moho depth (30 km) is 550ºC and surface heat flow is 50 mW m^{-2}. The top (0 ºC) and bottom (1300 ºC) temperatures are fixed as in the initial setup of the model.

2D Model setup

The two-dimensional model domain is 300 ×150 km with 450 × 240 linear, quadrilateral elements. Compositionally from to bottom, it has an "air" layer, upper crust, lower crust, and mantle from top to bottom. The air layer has a low density (0.01 kg/m^3) and relatively low viscosity (10^{18} Pa·s). The topography of the air-crust interface is assumed to be in an equilibrium state, which does not evolve with time, and the top of the air layer has an open surface, where materials are allowed to move in and out freely. The lower crust (between 15-30 km depth) is composed of two different materials. The stronger material (x = 150-300 km) is represented by plagioclase in Table S1, while the weaker material (x = 0-150 km) has an intrinsic viscosity that is 0.5, 0.1, 0.02 of the stronger material. A 3-km-wide weak zone (red in Fig. 3A in main text) extending from 2 km to 12 km below the surface at the midpoint of the model dips toward the stronger block at 63° with a frictional coefficient of 0.1. Other properties of the materials are the same as that in the three-dimensional model (Table S1). An inward velocity of 5 mm/yr, comparable with fault-normal convergent rate across SAF (Meade and Hager, 2005), is applied at the right boundary towards the left boundary, which is fixed (arrows in Fig.3). The temperature linearly increases from 0 $^\circ$C at surface to 600 $^\circ$C Moho depth (30 km depth) and then linearly increases to 1400 $^\circ$C at the thermal lithosphere-asthenosphere boundary (TLAB) at 80 km depth. An adiabatic temperature gradient of 0.5 $^\circ$C/km is applied to the mantle below the TLAB. The top and bottom temperatures are fixed as initial setup during model evolution.

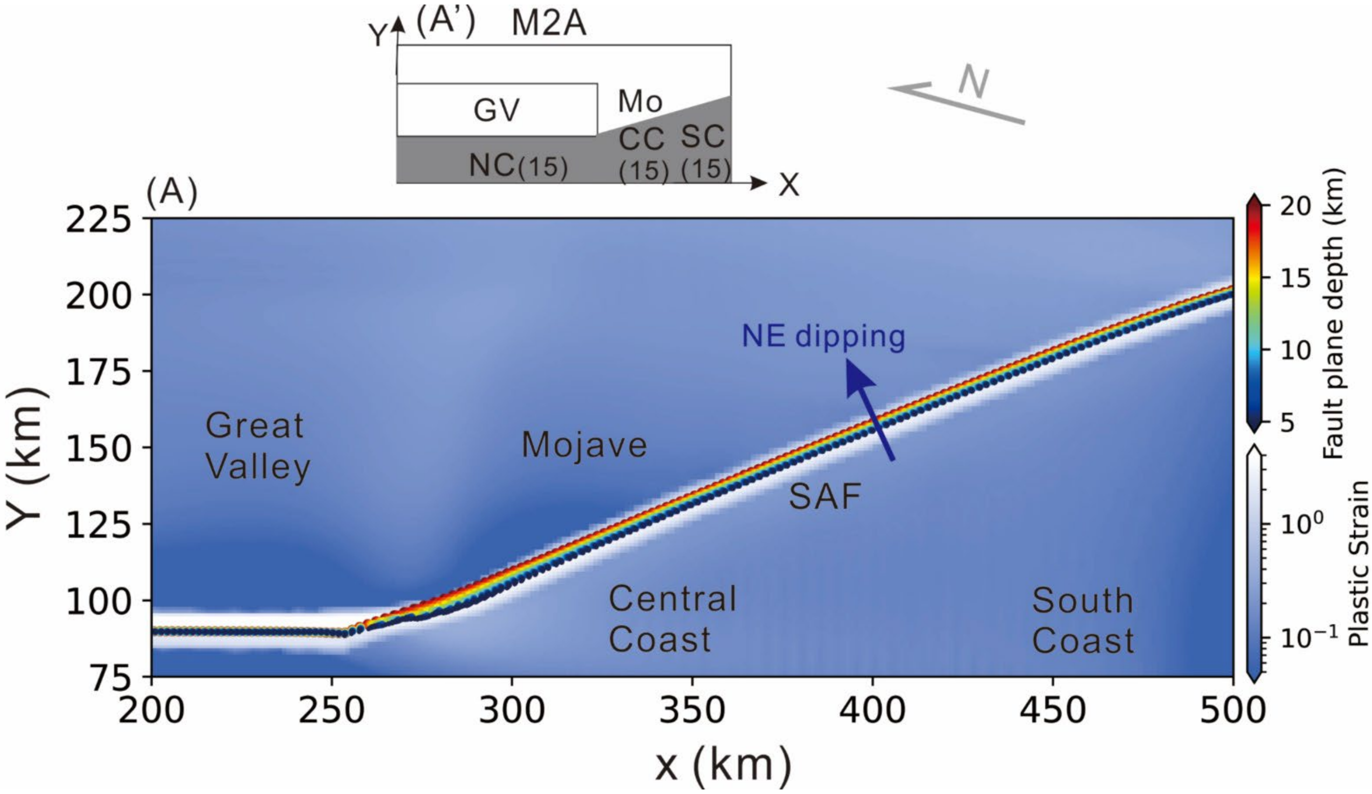

Figure S1. Snapshots of plastic strain distribution at a depth of 5 km and the fault plane depth distribution after 2.5 Ma for model M2A, which modifies M2 by replacing the plagioclase lower crust in the Great Valley with felsic lower crust. All other symbols are the same as that in Figure 2A-C in the main text. Replacing the mafic lower crust with felsic material in the Great Valley does not affect the NE dipping fault plane development in the M2, but the shear zone along the south edge of the Great Valley is not as localized as that in M2.

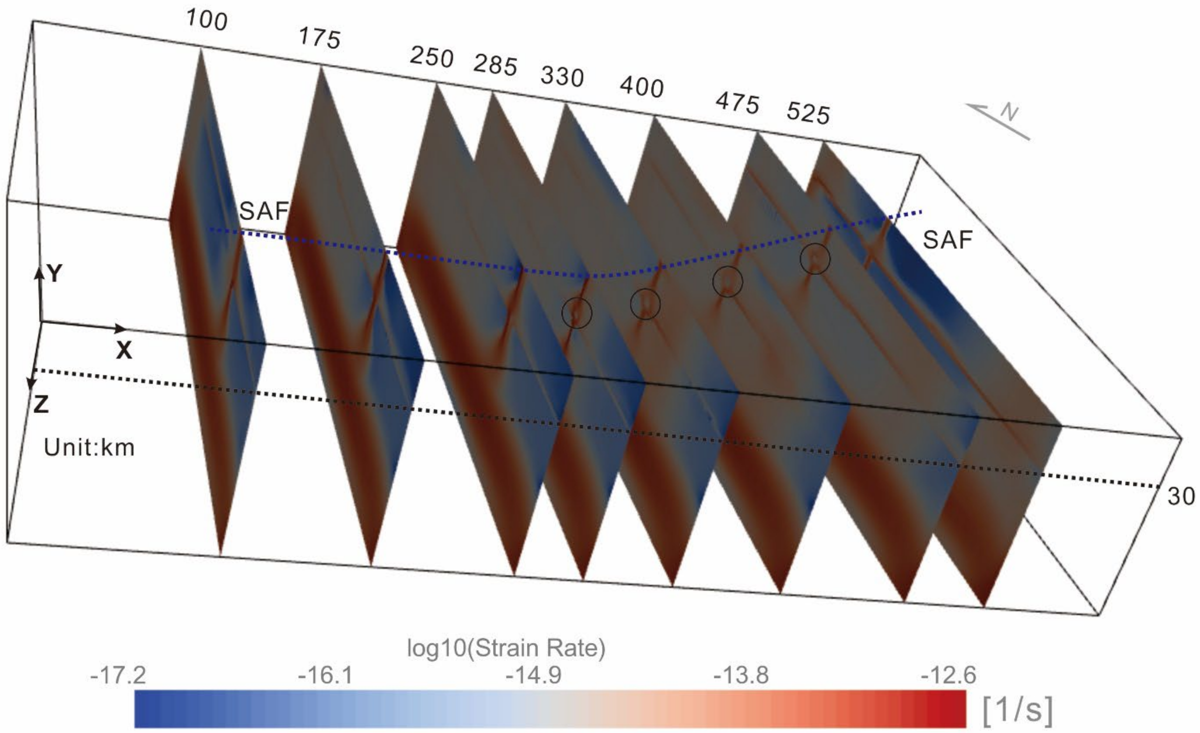

Figure S2. Second invariant value of strain rate for transverse profile along x-axis of M1. The symmetric features of deformation around SAF are marked with circles.

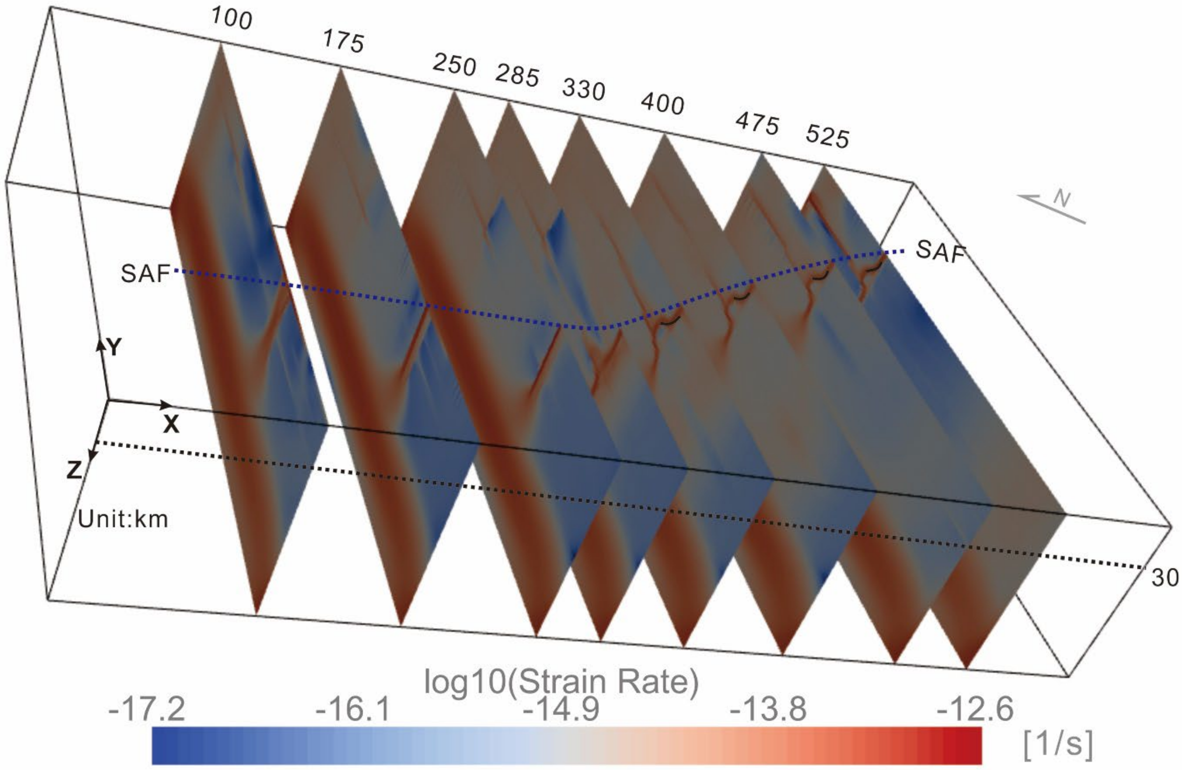

Figure S3. Second invariant value of strain rate for transverse profile along x-axis of M2. The asymmetric features of deformation around SAF are marked with black lines.

Tables

Table S1. Model arameters: The power law dislocation creep is in viscous regime is described as $\dot{\varepsilon} = A\sigma^n \exp\left(-\frac{E+VP}{RT}\right)$ where $\dot{\varepsilon}$ is strain rate, A material constant, σ deviatoric stress, n stress exponent, E activation energy, V activation volume, R the gas constant, and T temperature. The effective ductile viscosity $\eta = \frac{\sigma_{\mathrm{II}}}{2\dot{\varepsilon}_{\mathrm{II}}}$, where subscript marks the second invariant. Density $\rho = \rho_o[1-\alpha(T-T_0)]$, ρ_0 is the standard density at $P_O = 0.1$ MPa and $T_0 = 273$ K;Cp is heat capacity. α is thermal expansion. k is heat conductivity, and H_r radioactive heat production.

	Upper crust[1] (wet quartzite)	Lower crust[1] (plagioclase)	Mantle[2] (olivine)
A (MPa^{-n} S^{-1})	3.2×10^{-4}	3.3×10^{-4}	1.3×10^{6}
n	2.3	3.2	3.0
EkJ/mol	154	240	510
V(cm^3/mol)	0	0	14
ρ_o (kg/m^3)	2700	2900	3300
Cp (J/kg)	1200	1200	1200
α (K^{-1})	3×10^{-5}	3×10^{-5}	3×10^{-5}
k(W/mK)	2.5	3	3.5
H_r(μW/m^3)	2	0.1	0.01

[1] Ranalli (1995); [2] Karato and Jung (2003).

References

Atwater, T., and Stock, J., 1998, Pacific-North America plate tectonics of the Neogene southwestern United States: an update: International Geology Review, v. 40, no. 5, p. 375-402.

Burgmann, R., and Dresen, G., 2008, Rheology of the lower crust and upper mantle: Evidence from rock mechanics, geodesy, and field observations: Annual Review of Earth and Planetary Sciences, v. 36, no. 1, p. 531-567.

Collettini, C., Niemeijer, A., Viti, C., and Marone, C., 2009, Fault zone fabric and fault weakness: Nature, v. 462, no. 7275, p. 907-910.

Fliedner, M. M., Ruppert, S., Malin, P. E., Park, S. K., Jiracek, G., Phinney, R. A., Saleeby, J. B., Wernicke, B., Clayton, R., Keller, R., Miller, K., Jones, C., Luetgert, J. H., Mooney, W. D., Oliver, H., Klemperer, S. L., and Thompson, G. A., 1996, Three-dimensional crustal structure of the southern Sierra Nevada from seismic fan profiles and gravity modeling: Geology, v. 24, no. 4, p. 367-370.

Ford, H. A., Fischer, K. M., and Lekic, V., 2014, Localized shear in the deep lithosphere beneath the San Andreas fault system: Geology, v. 42, no. 4, p. 295-298.

Fuis, G. S., Ryberg, T., Godfrey, N. J., Okaya, D. A., and Murphy, J. M., 2001, Crustal structure and tectonics from the Los Angeles basin to the Mojave Desert, southern California: Geology, v. 29, no. 1, p. 15-18.

Glazner, A. F., Walker, J. D., Bartley, J. M., and Fletcher, J. M., 2002, Cenozoic evolution of the Mojave block of southern California: Geologic evolution of the Mojave Desert and southwestern Basin and Range: Geological Society of America Memoir, v. 195, p. 19-41.

Howie, J. M., Miller, K. C., and Savage, W. U., 1993, Integrated crustal structure across the south central California margin: Santa Lucia escarpment to the San Andreas fault: Journal of Geophysical Research: Solid Earth, v. 98, no. B5, p. 8173-8196.

Jones, C. H., Kanamori, H., and Roecker, S. W., 1994, Missing roots and mantle “drips”: Regional Pn and teleseismic arrival times in the southern Sierra Nevada and vicinity, California: Journal of Geophysical Research: Solid Earth, v. 99, no. B3, p. 4567-4601.

Karato, S. I., and Jung, H., 2003, Effects of pressure on high-temperature dislocation creep in olivine: Philosophical Magazine, v. 83, no. 3, p. 401-414.

Manley, C. R., Glazner, A. F., and Farmer, G. L., 2000, Timing of volcanism in the Sierra Nevada of California: Evidence for Pliocene delamination of the batholithic root?: Geology, v. 28, no. 9, p. 811-814.

Mansour, J., Giordani, J., Moresi, L., Beucher, R., Kaluza, O., Velic, M., Farrington, R. J., Quenette, S., and Beall, A. P., 2020, Underworld2: Python geodynamics modelling for desktop, hpc and cloud: Journal of Open Source Software, v. 5, no. 47, p. 1797.

Meade, B. J., and Hager, B. H., 2005, Block models of crustal motion in southern California constrained by GPS measurements: Journal of Geophysical Research-Solid Earth, v. 110, no. B3.

Mooney, W. D., and Weaver, C. S., 1989, Regional crustal structure and tectonics of the Pacific coastal states; California, Oregon, and Washington: Geological Society of America Memoirs, v. 172, p. 129-162.

Moresi, L., Quenette, S., Lemiale, V., Meriaux, C., Appelbe, B., and Mühlhaus, H.-B., 2007, Computational approaches to studying non-linear dynamics of the crust and mantle: Physics of the Earth and Planetary Interiors, v. 163, no. 1, p. 69-82.

Niemi, N. A., Buscher, J. T., Spotila, J. A., House, M. A., and Kelley, S. A., 2013, Insights from low-temperature thermochronometry into transpressional deformation and crustal exhumation along the San Andreas fault in the western Transverse Ranges, California: Tectonics, v. 32, no. 6, p. 1602-1622.

Popov, A. A., Sobolev, S. V., and Zoback, M. D., 2012, Modeling evolution of the San Andreas Fault system in northern and central California: Geochemistry Geophysics Geosystems, v. 13, no. 8, p. n/a-n/a.

Ranalli, G., 1995, Rheology of the Earth, Springer Science & Business Media.

Turcotte, D. L., and Schubert, G., 2002, Geodynamics, Cambridge university press.

Wang, K., Jiang, C., Yang, Y. J., Schulte - Pelkum, V., and Liu, Q., 2020, Crustal deformation in Southern California constrained by radial anisotropy from ambient noise adjoint tomography: Geophysical Research Letters, v. 47, no. 12, p. e2020GL088580.

Zhu, L. P., and Kanamori, H., 2000, Moho depth variation in southern California from teleseismic receiver functions: Journal of Geophysical Research-Solid Earth, v. 105, no. B2, p. 2969-2980.

Zoback, M. D., Zoback, M. L., Mount, V. S., Suppe, J., Eaton, J. P., Healy, J. H., Oppenheimer, D., Reasenberg, P., Jones, L., Raleigh, C. B., Wong, I. G., Scotti, O., and Wentworth, C., 1987, New evidence on the state of stress of the san andreas fault system: Science, v. 238, no. 4830, p. 1105-1111.